Developing the OSPREE Payload for Spectroscopic Measurements of a Mach 25+ Plasma Sheath

Ashwin P. Rao,* Jack D. Crespo,† Paolo Valentini,‡ Jonah B. Taylor,§ Vanessa J. Murray,¶ and Erin I. Vaughan**
Air Force Research Laboratory, Kirtland Air Force Base, New Mexico 87117
and
Robert Alviani†† and Marat Kulakhmetov‡‡
Varda Space Industries, El Segundo, California 90245

https://doi.org/10.2514/1.A36325

Sensing atomic and molecular emissions from the radiant plasma sheath that forms around reentry spacecraft will advance the understanding and modeling of high-enthalpy flows. Optical emission spectroscopy (OES) measurements in this extreme environment can yield data needed to anchor aerothermal flow models in the Mach 20+ regime. This paper presents the development of an OES payload for a commercial reentry capsule, composed of commercial-off-the-shelf hardware modified for spaceflight. The flight-qualified sensor will yield novel optical emission spectra of the reentry plasma sheath from 350 to 800 nm, providing invaluable data characterizing the dynamic aerothermal chemistry of this unique environment. We present an overview of the sensor payload design and planned reentry experiment. The simulation of the sensor response in key flight regimes is presented from direct simulation Monte Carlo and computational fluid dynamics output coupled to the NEQAIR radiative emission tool, allowing for preflight understanding of the dynamic emissions of N_2, N_2^+, O_2, O_2^+, N, N^+, O, O^+, NO, and NO^+ species that manifest in the plasma sheath.

I. Introduction

SPACECRAFT reentering the Earth's atmosphere experience an extreme environment characterized by uniquely complex chemistry and aerothermodynamics. Reentry vehicles reach the upper atmosphere at Mach numbers above 25, creating a bow shock that heats the surrounding air to temperatures in excess of 15,000 K. Shocks are most efficient at converting the kinetic energy of the gas into translational thermal energy. As a result, the high-enthalpy flow in the shock layer is characterized by significant thermal nonequilibrium [1–4]. Furthermore, the temperatures in the shock layer are sufficient to dissociate molecular nitrogen and oxygen and induce ionization, forming a plasma sheath [5,6]. These thermochemical nonequilibrium processes affect vehicle aeroheating, surface pressure distributions, and flowfield chemical species concentrations. These parameters, in turn, are of consequence to vehicle thermal protection system (TPS) performance, aerodynamic stability, and performance of sensing and communications systems during flight. Ground test facilities are currently unable to accurately replicate hypersonic flows past Mach 12, and hypersonic flight tests dedicated to fundamental scientific measurements in these Mach regimes have been infrequent. Thus, most high-enthalpy thermochemical relaxation and dissociation models remain highly uncertain and lack proper validation data [7–9]. Fielding surface probes on a reentry vehicle to collect such data could negatively affect vehicle aerodynamics, and survivability of such instruments in the plasma sheath is tenuous. However, excited chemical species in the plasma generate radiant emissions across the ultraviolet (UV), visible (Vis), and near-infrared (NIR) spectrum, which can be measured using optical emission spectroscopy (OES) techniques. Recorded spectra can be analyzed to determine species densities, time-evolving chemical species kinetics, gas temperatures, and internal energy state populations. In-flight OES measurements can be implemented to nonintrusively measure shock layer aerothermal chemistry and generate validation data for high-enthalpy flow models in reentry regimes.

Historically, scientific efforts fielding OES systems on high-speed vehicles have been few and far between. The 1990 and 1991 bow shock ultraviolet 1 and 2 (BSUV-1 and BSUV-2) tests recorded emission spectra between 200 and 400 nm by fielding an optical emission spectrometer on a sounding rocket, recording between altitudes of 37 and 75 km at 3.5 km/s (Mach 11) [10,11]. These tests captured vital spectral emission information related to chemical processes that occur in the plasma sheath, such as the formation of OH A-X, NO γ, and N_2^+ systems [12–14]. Experiments fielding OES systems during true orbital reentry are even sparser in the literature. The Kentucky Reentry Universal Payload System (KRUPS) team successfully reentered a set of compact, nonrecoverable capsules deployed from the ISS resupply vehicle Cygnus during the KREPE-2 flight test [15]. These capsules contained a miniature Hamamatsu spectrometer with a range from 340 to 850 nm and were estimated to reach a peak Mach number of 20. However, the bandwidth limitations of the Iridium network telemetry system forced the data to be collapsed into six color bins, and fully resolved spectra of the reentry plasma could not be transmitted [16]. The European Space Agency (ESA) developed the European eXPErimental Reentry Testbed (EXPERT) vehicle for in-flight reentry experimentation and data collection, validation of computational models, and flight qualification of novel sensing systems [17]. One of the sensors developed was the REentry SPECTrometer (RESPECT) system, which sought to obtain OES measurements of the reentry plasma between 200 and 900 nm from altitudes of 35 to 70 km as the EXPERT vehicle reached speeds up to 6 km/s (Mach 17) [18]. RESPECT used a modified Ocean Optics S2000 miniature spectrometer, connected via fiber optic cables to optical apertures in the nose

Presented as Paper 2024-4560 at the AIAA Aviation Forum 2024, Las Vegas, NV, July 29–August 2, 2024.; received 29 November 2024; accepted for publication 15 February 2025; published online 5 March 2025.

*Section Chief, AFRL/RV; ashwin.rao.1@us.af.mil. Young Professional AIAA.
†Associate Research Engineer, AFRL/RV. Student Member AIAA.
‡Senior Research Engineer, AFRL/RV. Member AIAA.
§Plasma Physicist, AFRL/RV. Young Professional AIAA.
¶Experiments Lead, AFRL/RV.
**Aerodynamics Engineer. Young Professional AIAA.
††Prometheus Testbed Lead, AFRL/RV.
‡‡Head of Analysis and Hypersonics. Young Professional AIAA.

cap and forebody. The ESA conducted a computational analysis of the sensor response and designed engineering and flight models to be qualified, targeting a flight test in early 2007 [19]. Unfortunately, the test was canceled due to issues with the launch provider, and the vehicle has been in storage since 2014.

The historical lack of *in situ* spectral-sensing experiments in the reentry environment can be overcome by the recent explosive growth of the American space industrial base. On 21 February 2024, Varda Space Industries, an American space startup, became the first commercial U.S. space entity to land a reentry capsule on American soil in a history-making mission. While Varda's commercial mission is to produce pharmaceuticals in microgravity and return them to Earth, their operations provide an avenue for external customers to use their capsule as a high-fidelity testbed to perform experiments in the reentry environment. This paper presents the design, development, and qualification of the Optical Sensing of Plasmas in the ReEntry Environment (OSPREE) payload, which has been integrated into Varda's W-2 capsule for a reentry mission in early 2025 [20]. This experiment will collect Vis-NIR radiative emissions from within the capsule during its descent to Earth at speeds up to Mach 29, providing novel and groundbreaking OES data about this uniquely extreme environment. We present an overview of the OSPREE experiment, sensor design, and computational methods implemented to simulate the sensor response along W-2's reentry trajectory.

II. Spacecraft Design and Measurement Principle

Varda produces a blunt-body, ballistic, 1-m-diam reentry capsule, shown in Fig. 1a. The capsule is designed to be self-stabilizing and survive the harsh reentry environment. The forebody is outfitted with a NASA conformal phenolic impregnated carbon ablator (C-PICA) TPS, while the aft dome is covered with a nonablative TPS material. The aft dome also contains pocketed areas where optical windows can be integrated into the capsule, one of which is seen in Fig. 1. Internally, the capsule contains the avionics system and payload mounting deck, shown in Fig. 1b, where the OSPREE system will be attached. Optical sensing can be conducted through the aft dome windows, as demonstrated by the recovered and publicly available GoPro footage from the first reentry mission [21]. A still frame of this footage is shown in Fig. 2, demonstrating that the plasma sheath and effects of ablation can be observed by sensors conducting measurements from this window.

OES measurements can be implemented by mounting a collimating lens against the inside of this window, with a line of sight (LOS) directly into the flowfield, which travels around the shoulder and aft dome of the capsule. This yields optical emission spectra from the various excited species in the plasma, providing valuable information about the evolving aerothermal chemistry during reentry. This aft dome LOS measurement, explained further in Sec. IV.A, was favored due to the preexisting inclusion of the optical window in the capsule design and the mission risks inherent in placing an optical aperture in the forebody. The forebody sees much higher heat fluxes than the shoulder region, introducing complexities such as the need for cooling the collection optics and ensuring matched coefficients of thermal expansion between the TPS and optical aperture. Failure of the optic in the forebody would have catastrophic results on the mission and risk the commercial pharmaceutical manufacturing payload also in the capsule. Thus, obtaining measurements from the existing window location was deemed the best course of action with less risk. Further sensing experiments aiming to take leading-edge spectral measurements will benefit from the data collected during this initial proving experiment and the lessons from the engineering efforts undertaken. Successful performance of OSPREE will validate the design and components for use in reentry, and the measurements obtained from the aft dome will help scope saturation limits of the detector. Since plasma radiance is expected to be stronger around the forebody, the effects of exposure time and additional noise on the recorded spectra must be considered. The W-2 flight data will help identify necessary changes to integration time sampling and requirements for filters or other optics, which may be needed for forebody measurements.

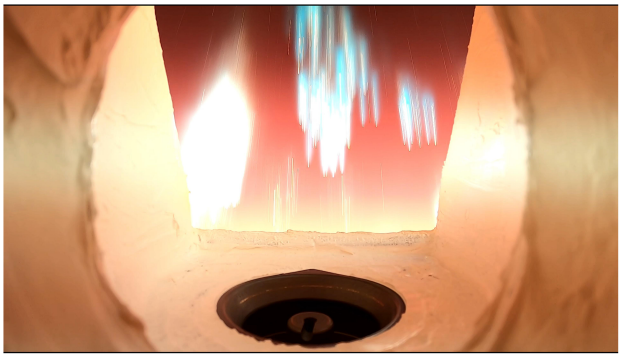

Fig. 2 Frame of reentry footage showing radiating orange-red plasma from surrounding airflow as well as glowing debris from C-PICA ablation [21].

III. OSPREE Design, Qualification, and Operation

A. System Components

The main component of the OSPREE payload is the Ocean Optics HR2 Vis-NIR spectrometer, identified in Figs. 1b and 3a. A commercial spectrometer was chosen because its low cost and adaptability fit within the financial and time constraints of the development window for the mission. Additionally, the RESPECT system used a modified Ocean Optics S2000, indicating prior utility of these units in spaceflight applications [18,19]. The design and operation parameters of the spectrometer are listed in Table 1. The sub-1-nm resolution of the HR2 is ideal for this application, as it can adequately capture major atomic and molecular emissions in the reentry plasma across a wide spectral range.

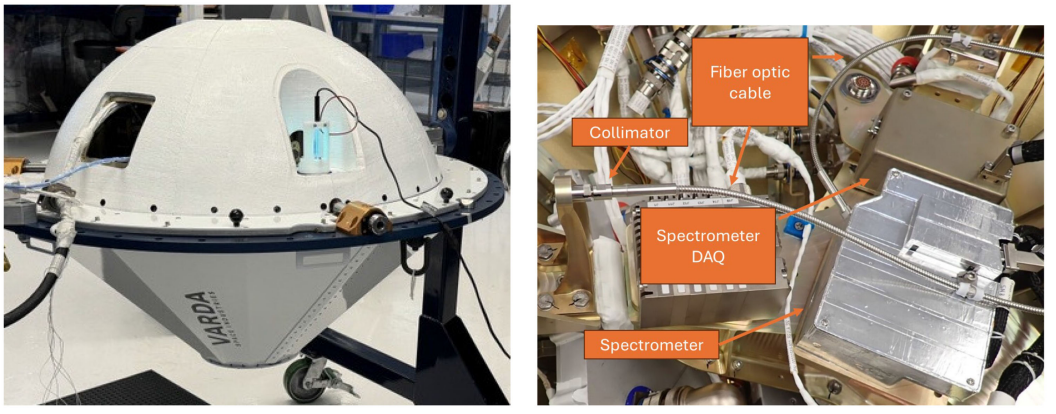

a) b)

Fig. 1 Varda reentry capsule containing OSPREE: a) external structure and b) internal view of payload mounting deck with OSPREE components.

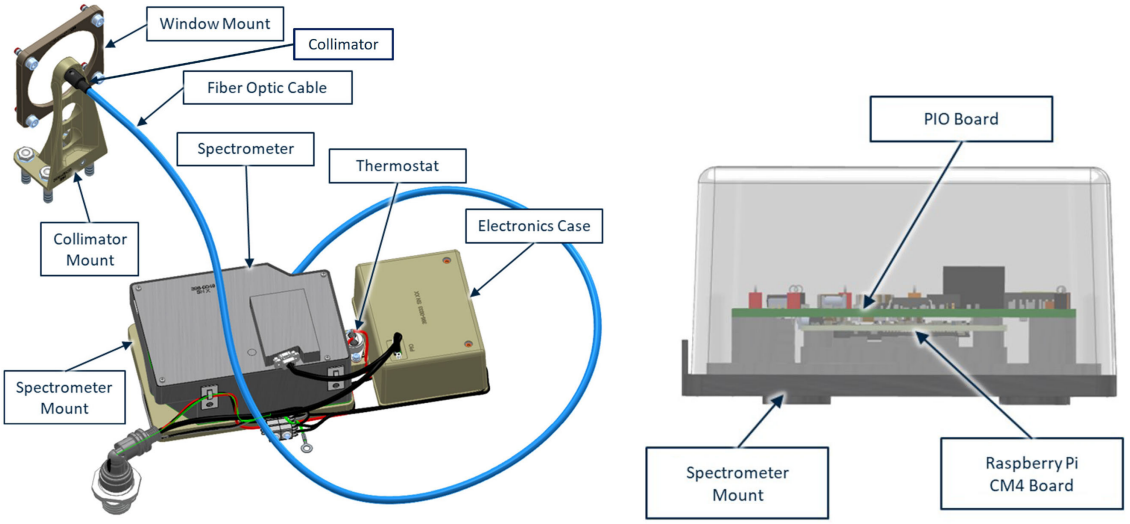

Fig. 3 a) Main sensing payload hardware components and b) contents of electronics box.

The optical system was also chosen from commercial parts, composed of an Accuglass high-temperature and vacuum-rated collimating lens and a Thorlabs MFV1L1 steel-jacketed 100-μm-diam InF_3 optical fiber also rated for high-vacuum conditions. A threaded mount was designed for the collimator, ensuring that the lens could be fixed as close to within the allowable tolerances of the optical window as possible. The collimator has an effective light spot diameter of 4.06 mm and was sufficient to capture emissions from a low-intensity calibration lamp placed at the capsule shoulder during integration and testing, as shown in Fig. 1a. The footage recorded by a simple commercial camera during the February 2024 reentry event indicated no evidence of potential damage or distortions to the window from the thermal environment, likely due to its position in the aft dome pocket. In addition, no ablation debris was deposited on the window, ensuring a clear field of view and unimpeded optical transmission during reentry. This greatly reduced the risk of using a collimating lens in this particular position and negated the need to perform thermal simulation analysis of the window, as is needed for optical apertures in locations that experience higher heat loading.

The second main part of OSPREE is the electronics box, shown in Fig. 3b. A Raspberry Pi Compute Module 4 (RPi CM4) was chosen as the flight computer and data acquisition (DAQ) system. RPis have a history of space utility, with many prior experimental efforts demonstrating that they are robust enough to survive the space environment [22]. The compact size and low power draw of the CM4 are ideal for this application, as well as its embedded multimedia card (eMMC) memory. This removes risks of file corruption associated with saving data on a removable SD card. A custom I/O board was fabricated to serve as the electronic interface between the capsule electronics, CM4, and spectrometer. The board provides power to the system, while also allowing for I/O pin triggering of the entire payload from the capsule's avionics.

Table 1 Ocean Optics HR2 spectrometer unit key parameters

Parameter	Value
Spectral range	350–800 nm
Resolution	$\Delta\lambda = 0.23$ nm
Blaze	400 nm
Groove density	600 g/mm
Slit width	10 μm
Detector	2098 pixel CCD
Exposure range	1 μs–2 s
Dimensions	$149 \times 106 \times 48$ mm
Weight	931 g

B. Software and Avionics

Another advantage of the HR2 spectrometer is that the OceanDirect software development kit (SDK) is i) compatible with Python and ii) capable of being installed on ARM64 devices, such as RPis. A simple Python script was developed to control and operate the payload system during reentry, shown in Fig. 4a. The control script on the CM4 runs as soon as the system is powered on and waits for a voltage signal on a particular I/O pin, using the RPi.GPIO Python functions. These signals are provided by load channels connected to the capsule's main power and are programmed to trigger a set duration of time after the capsule separates from the satellite bus. When the pin is triggered, the control script activates the spectrometer through the SDK functions and initializes the recording sequence, saving the recorded wavelengths and intensities of each recording on the eMMC. A watchdog circuit connected to the I/O board monitors the system for power interruptions and triggers a smoother system restart in case of an upset event.

Figure 4b shows the overall structure of the capsule and payload avionics and the three main load channels that operate the OES system. Load channel 1 provides power to the PIO system through the watchdog circuit, while channel 2 provides the sync signal telling the CM4 to initiate the spectrometer recording. A third load channel is used to power a heater attached to the underside of the spectrometer; the spectrometer temperature is monitored by two resistance temperature detectors (RTDs) while the capsule orbits. The heater circuit is turned on before the capsule is separated from the satellite bus, ensuring that it is at the minimum operational temperature of 0°C.

C. Modifications for Flight Qualification

The extreme nature of the low Earth orbit (LEO) and reentry environments necessitated modifications of the COTS payload hardware and spaceflight qualification testing of the assembly. This ultimately ensures payload survivability and reduces the risk of catastrophic payload failures that could jeopardize other systems in the reentry spacecraft. Per the integration compliance requirements of the capsule provider, the OSPREE system underwent three major qualification events: i) tri-axis random vibration, ii) thermal vacuum (TVAC), and iii) electromagnetic interference (EMI) testing. Modifications to the COTS payload components allowed the assembly to successfully complete the environmental testing and meet do-no-harm requirements.

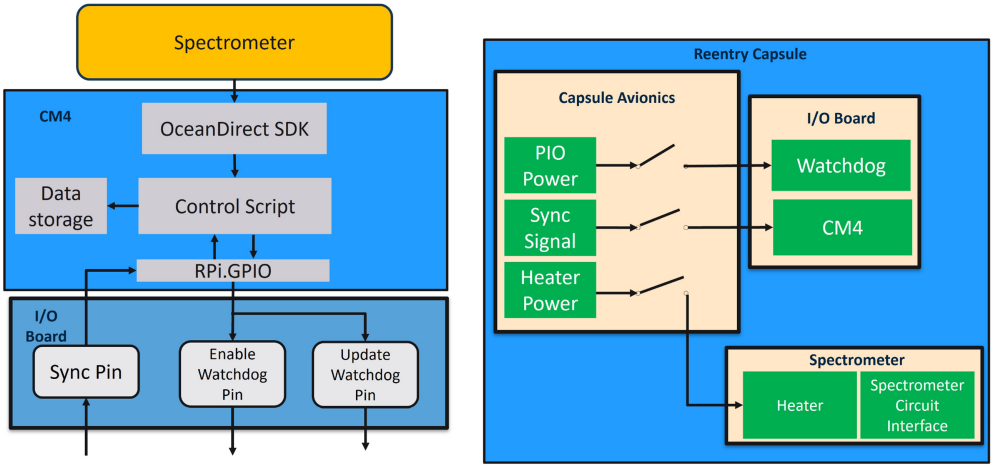

a) b)

Fig. 4 Flow diagram showing operations for a) software controller program and b) capsule avionics and payload system communication.

The most extensive modifications were made to the HR2 unit itself. Firstly, the outer chassis of the spectrometer case was removed completely to reduce total system mass, leaving just the inner aluminum casing. The stock lid of the casing was also discarded, and a custom lid was manufactured, which included a port for a micro-D cable and a venting hole for thermal vacuum and bakeout. This allowed power and I/O connections to be hardwired directly into the HR2 circuit board rather than using the stock USB-C and 15-pin connector ports, which are not reliable in a vibration environment. Additionally, a heater pad was installed at the bottom of the spectrometer casing, along with a resistance temperature detector (RTD). This system monitors the temperature of the spectrometer and powers on the heater to keep the HR2 above its minimum storage (−30°C) and operational (0°C) temperatures. No major modifications to the RPi CM4 were made aside from the application of a conformal coating, and the connections to provide I/O signal and power to the HR2 were directly soldered onto the PIO board. Additionally, all wireless connectivity functions on the CM4 were disabled to comply with the SpaceX Rideshare Payload User's Guide (RPUG) radio frequency requirements and pass EMI testing. No modifications to the optical system were made since the collimator and fiber were both designed for vacuum and high-temperature environments.

D. Experiment Concept

Figure 5 depicts the notional timing sequence of major events during reentry related to the operation of the OSPREE payload. All timing signals are synced to the time postseparation. The spectrometer is powered on approximately 6 min after the capsule separates from its satellite bus and waits for the sync load signal to begin recording 10 min postseparation. The system will record data for approximately 4 min until the sync load switch is powered off to end data collection. These timing intervals correspond to an altitude range of 100 km down to 40 km, where the plasma is expected to manifest based on the W-1 recording. The timing was correlated to altitude based on trajectory data collected from the W-1 capsule. The payload is then powered off 15 min postseparation to prepare for parachute deceleration and landing. Upon landing, the capsule will be recovered for payload extraction, after which the data from the RPi system will be removed for postflight analysis.

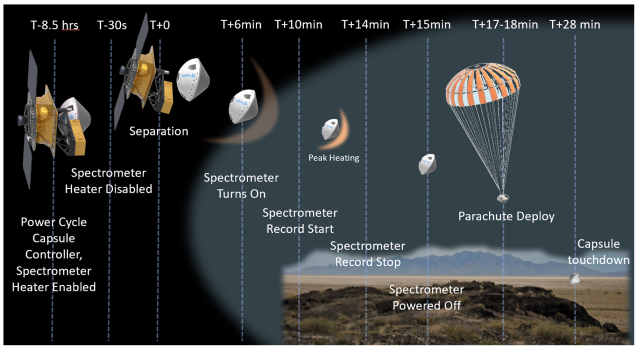

Fig. 5 Reentry mission event sequence for OSPREE payload.

IV. Computational Results and Determination of Simulated Sensor Response

During the development of the payload, it was determined that simulating the sensor response to the flowfield at various trajectory points would greatly reduce uncertainty in payload performance and help ascertain proper values for spectrometer integration time to record a correctly exposed signal. Thus, a computational campaign was initiated to gather and analyze this data, similar to the work conducted for the RESPECT system [19]. Firstly, the reentry flowfield was simulated computationally to calculate key parameters such as temperatures and species densities, which affect the spectral radiance of the plasma. Next, a radiative solver was used to calculate a synthetic emission spectrum based on the previously determined flowfield properties. Finally, the synthetic spectrum was converted to payload response by using conversion functions at varying integration times for the spectrometer measured in the laboratory. This provided critical information about the notional sensor response along the trajectory and bounded the integration times programmed into the payload software.

A. Computational Methods: DSMC and CFD

Thermochemical nonequilibrium simulations of the flowfield around the capsule at various trajectory points were performed using the Stochastic PArallel Rarefied-gas Time-accurate Analyzer (SPARTA) DSMC solver [23], as well as the Langley Aerothermal Upwind Relaxation Algorithm (LAURA) CFD solver [24]. Six trajectory points were chosen, listed in Table 2 with corresponding altitudes (z), Mach numbers, freestream velocities (v_∞), freestream densities (ρ_∞), freestream temperatures (T_∞), and Knudsen numbers (Kn).

The DSMC method is a Lagrangian particle method that is applicable to simulating gas flows at dilute conditions [25]. The gas is represented by *simulator* particles advected through the flow domain by using their center-of-mass velocity. Collisions between particles cause momentum and energy transfers. External (translational) and internal (rotational, vibrational, electronic, etc.) energy exchanges are modeled as well. DSMC simulations are time-advanced using a time step of the order of the shortest mean collision time occurring in the flow. The spatial domain is discretized in control volumes (cells) whose size is a fraction of the local

Table 2 Trajectory points of the Varda testbed vehicle chosen for simulation analysis

z, km	Mach	v_∞, m/s	ρ_∞, kg/m^3	T_∞, K	Kn	Method
98.2	28.4	7921.3	7.92e−7	188.2	10^{-1}	DSMC
85.5	28.0	7920.0	7.93e−6	198.0	10^{-2}	DSMC
70.0	26.5	7738.0	7.95e−5	221.2	9.7×10^{-4}	CFD
58.0	21.5	6849.8	4.16e−4	251.9	2.0×10^{-4}	CFD
51.7	20.1	5752.1	8.88e−4	266.4	8.1×10^{-5}	CFD
47.5	13.4	4438.4	2.88e−3	269.4	4.8×10^{-5}	CFD

Higher altitude points in rarefied flow conditions were run using SPARTA, while lower altitude points in continuum flow conditions were run using LAURA. The Knudsen number (Kn) is based on the freestream mean free path and the capsule diameter.

mean free path. Unlike standard molecular dynamics techniques, each cell only contains a fraction of the total number of real molecules that would have been present based on the local mass density. A particle weight is used as a ratio between the simulator and *real* particles. The no-time counter algorithm of Bird [25] is used to select the collision pairs in each cell at every time step.

In the simulations presented in this work, the variable hard-sphere (VHS) model is used to describe the viscosity cross-section. The VHS parameters were set based on viscosity data obtained from previous first-principles calculations [26]. The internal energy relaxation kinetics are modeled using the so-called collision numbers. A fixed relaxation number for rotation was set to 5 [27]. The temperature dependence of the vibrational relaxation number was instead modeled according to Bird [25] and parameterized based on the *ab initio* quasi-classical trajectory analyses of Torres et al. [28]. Rotational and vibrational modes of *both* colliding particles are relaxed during the collision. The Borgnakke–Larsen model [25] is used for internal energy redistribution. The reacting, ionized air mixture contains 11 species, namely, N_2, O_2, NO, N, O, N_2^+, O_2^+, NO^+, N^+, O^+, and e^-. All are assumed to be in their ground electronic state. The ambipolar approximation [29] is used to model electron transport across the flow. No external electric or magnetic fields are included in the simulations. The total collision energy model [25] is used to compute the probability of a chemical reaction occurring during a collision. The set of reactions that are used to model the ionized flow and resulting plasma sheath are from the work of Farbar et al. [30]. Due to the strong density gradients across the flowfield, grid adaptation is needed in order to guarantee that the *mean collision separation* is a fraction of the local mean free path [25]. In the SPARTA code, an octree automatic mesh refinement process is used to ensure each collision cell has a size that does not exceed the local mean free path evaluated based on the VHS collision cross-section model. A total of 6 and 5 refinement levels had to be used for the 85 km and the 98 km cases, respectively. The resulting number of collision cells was about 65 million for the 85 km case and 8 million cells for the 98 km case. A conservative time step of 0.1 μs was used in the simulations. Preliminary validations against previously published data on the RAM-C II flight experiment were conducted to assess the overall fidelity of the selected DSMC models. Good agreement was found with both experimental and computational data for electron number densities along the RAM-C II geometry [30,31].

Although accurate at near-continuum conditions, the DSMC method is generally used for rarefied and transitional flows. Here, the two highest trajectory points at 98 and 85 km were run using SPARTA. In both cases, the simulations were three-dimensional, and half of the capsule was modeled at a zero angle of attack. Up to 2 billion particles were used in the simulations. As these flows are only weakly ionized, an accurate estimation of *trace* species, such as electrons, requires a large number of particles to reduce the statistical uncertainty. Samples were collected over 10,000 time steps after the system had reached a steady state. We verified that the electron number densities at various locations around the capsule were independent of the number of particles used in the simulation. The wall temperature was set to 300 K.

The rest of the trajectory points were computed with NASA's LAURA solver. These cases were set up with laminar flow conditions using an 11-species (N_2, O_2, NO, N, O, N_2^+, O_2^+, NO^+, N^+, O^+, e^-), two-temperature ($T_{tr} = T_r \neq T_v$) air chemistry model with thermochemical nonequilibrium. In this two-temperature model, the translational and rotational temperatures are assumed to be in equilibrium, while the vibrational temperature is solved. The wall boundary conditions are specified as super-catalytic walls in radiative equilibrium at a temperature of 2000 K. This thermochemical model was validated against published simulations of the RAM-C II flight experiment and was found to agree very well. The spatial domain is created with 48 3D blocks for parallel computation with the LAURA solver. Each block is dimensioned to include 128 cells in the wall-normal direction. Varying axial and circumferential dimensions maintain a roughly uniform cell size and sufficiently refined regions of smaller length scales to mitigate numerical diffusion. LAURA's automatic shock-alignment mesh-adaption algorithm was used to align the mesh to the shock wave and adapt the wake region.

Flowfield species number densities and temperatures along the optical LOS were extracted from each solution; this LOS, shown in Fig. 6a, represents the optical path within the flowfield in line with the collimator. The translational and vibrational temperature contours at 58 km are shown in Fig. 6b. Figures 7a and 7b show the

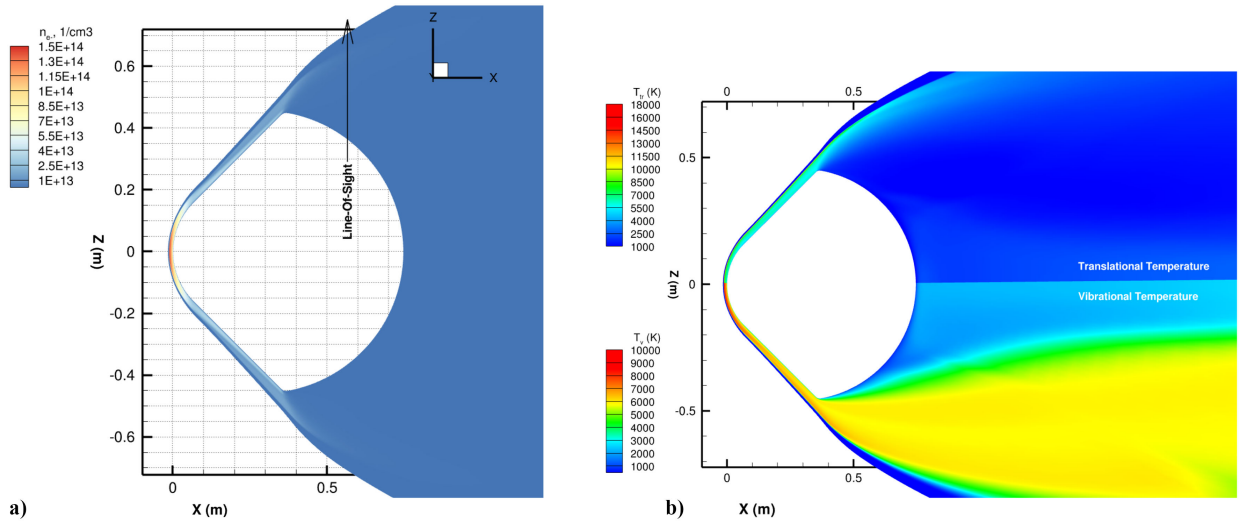

Fig. 6 LAURA flowfield solution showing the a) electron number density and b) translational-rotational and vibrational temperatures at 58 km.

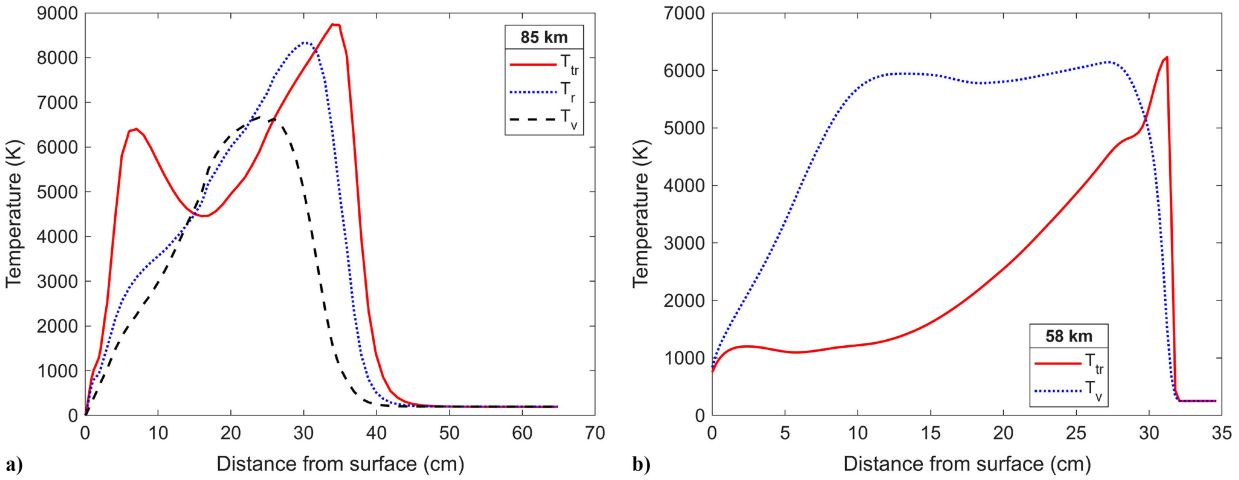

Fig. 7 Temperature variations along optical LOS at a) 85 km and b) 58 km. Note that (b) was generated using LAURA's two temperature model, and thus $T_{tr} = T_r$.

temperature distributions along the LOS at 85 km extracted from DSMC and at 58 km (peak heating) extracted from LAURA. At 85 km, the translational temperature drops quickly between the shock front and the vehicle's surface. This is due to the strong expansion in the wake. The second peak is due to a weak recompression near the wall. The rotational and vibrational temperatures lag the translational temperature and remain frozen due to rarefaction effects in the wake. At peak heating (58 km), the vibrational temperature similarly lags the translational temperature as the gas crosses the oblique shock at a distance from the surface of about 32 cm. Again, the presence of a strong expansion region results in a vibrationally frozen flow in the wake, manifested by a vibrational temperature significantly larger than the translational temperature. Final thermal equilibration is then observed at the wall. These trends are also observed at the peak dynamic pressure point in the trajectory but are significantly less pronounced, as internal temperatures equilibrate with the translational temperature within 15 cm from the surface. This expectedly suggests that vibrational nonequilibrium is more pronounced at conditions corresponding to higher altitudes (rarefaction effects) and higher Mach numbers (large freestream enthalpies).

Figures 8a and 8b show the species number density profiles along the LOS at 85 and 58 km. At 85 km, N_2 and O_2 are prevalent across the LOS. while N, O, and NO drop off in the expansion region, indicating that the molecular dissociation reactions forming neutral atomic species are predominantly occurring within 30 cm of the capsule surface. Neutral species dominate the overall population, as ionization is minimal based on the six-order-of-magnitude difference in number density between neutral and ionized constituents. At peak heating, N, O, and N_2 are the most prominent species in the shock layer across the LOS; the five-order-of-magnitude difference between NO_2 and NO indicates the dominance of oxygen dissociation reactions in this region at 58 km. Appreciable quantities of singly ionized NO and O are present, but overall the ionized species densities at this trajectory point are negligible compared to their neutral counterparts.

B. Simulation of Spectral Radiance

A data file was generated containing the LOS distance (cm), species number densities (cm^{-3}), and temperatures (K) at each extracted LOS point. This LOS input file was fed into NASA's NEQAIR v15.2 radiative emission code to calculate the spectral radiance along the optical LOS for wavelength values between 346.5 and 807.2 nm with a spectral grid spacing of 0.2184 nm. These numbers correspond to the wavelength range and resolution of the OSPREE payload. Since the flow around the capsule was assumed to be in a state of chemical nonequilibrium, the atomic and molecular excited state populations could not be expected to follow a Boltzmann distribution. As a result, NEQAIR was run in its non-Boltzmann state population mode that uses a collisional-radiative (CR) interaction model to determine excited electronic state populations for each species. An LOS geometry was specified in the input file, as OSPREE uses a collimator with a 4.06-mm-diam effective light spot. Thus, this geometry was selected to most closely resemble the payload optics. Figure 9a contains the computed spectral radiance across the OSPREE wavelength range for each of the trajectory points in Table 2. The emitted spectral radiance is

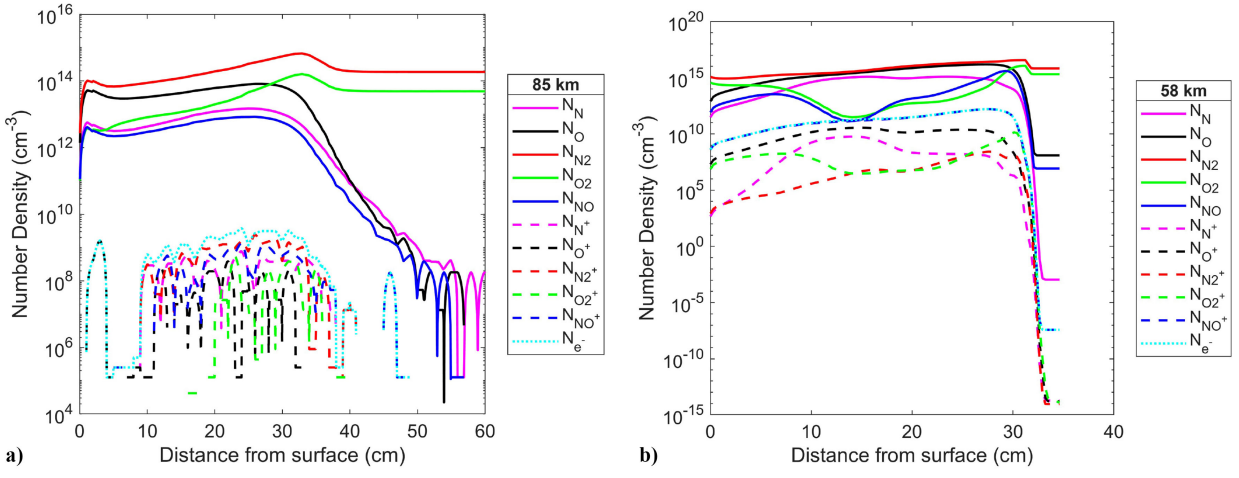

Fig. 8 Species number density variation along LOS at a) 85 km and b) 58 km.

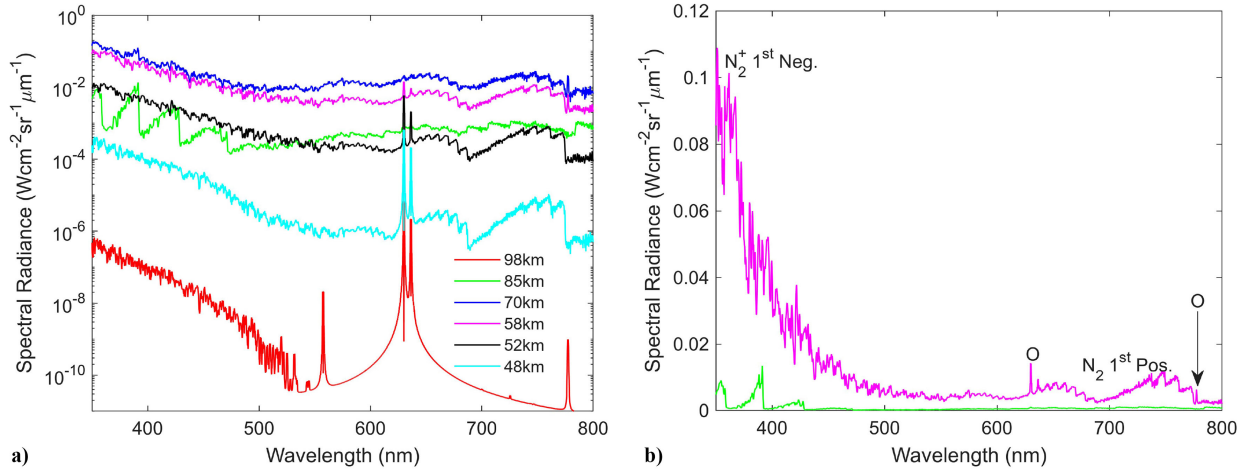

Fig. 9 Computed spectral radiance along optical LOS from 350 to 800 nm for a) all simulated trajectory points and b) 85 and 58 km with labeled emission features.

minimal at the 98 km (red) trajectory point, which is expected due to the low air density and rarefied flow conditions. Atomic emission peaks are seen in the computed spectrum, although these would likely not be detectable by a sensor at these magnitudes. As the capsule descends to 85 km (green) and the freestream density increases by an order of magnitude, the emitted spectral radiance increases by around four orders of magnitude. Emission features of molecular nitrogen bands begin to appear, indicating increased excitation of these species.

As the capsule descends further into the continuum flow region at 70 km (blue), radiance increases by another order of magnitude. In addition to the continued presence of emissions from molecular nitrogen, the first clear indication of atomic O is seen at 777 nm, indicating a strong prevalence of oxygen dissociation reactions occurring in the plasma. At 58 km, additional atomic O emission peaks manifest at 630 and 636 nm, which increase in strength relative to the present molecular emissions as the capsule slows to Mach 20 at 52 km. Between 52 and 48 km, the capsule decelerates drastically to Mach 13, approaching the lower limit of the high hypersonic regime. During this period, the computed radiance falls nearly two orders of magnitude as the maximum temperature along the LOS decreases to 3000 K. Based on the flowfield temperatures and computed radiance values, it is expected that the plasma sheath ceases to exist beyond this trajectory point. Figure 9b isolates the 85 and 58 km radiances; the N_2^+ first negative and N_2 first positive systems between 350 and 500 nm and between 650 and 750 nm are labeled, along with the atomic oxygen peaks at 630, 636, and 777 nm.

To further understand the computed spectra, we compare the selected trajectory points with footage taken by a commercial camera along the LOS during the 2024W-1 reentry event. Figures 10a–10f show still frames from the reentry between 95 and 50 km. The heat pulse is first noticeable around Fig. 10a; the glow indicates the beginning of molecular N_2 and O_2 excitation in the flowfield. The radiance increases and the plasma begins to glow orange as the capsule descends to 70 km in Figs. 10b–10d, correlating to the radiance increases seen in Fig. 9 and the presence of atomic O emissions indicating molecular dissociation. It should be noted that around 70 km, ablation of the TPS forebody began, and ablated material radiating white-hot is evident in the plasma. Ablated debris initially manifests in large pieces but begins to spall as the capsule approaches peak heating, as seen in Fig. 10e. A separate study is being conducted to examine ablation effects on the flowfield chemistry of this capsule, but no ablation modeling at these lower altitudes was conducted to scope the development of OSPREE. It is expected that the spectra recorded within this portion of the trajectory will contain portions of molecular emission bands from CN-violet (350–422 nm), C_2 Swan (440–565 nm), and CH (425–435 nm), as well as atomic emission lines from H (468 and 656 nm) due to the chemical interactions between the TPS and shock-heated air. These emissions will likely overlap or interfere with N_2 emissions from the air; the degree of this interference will be dependent on the number densities

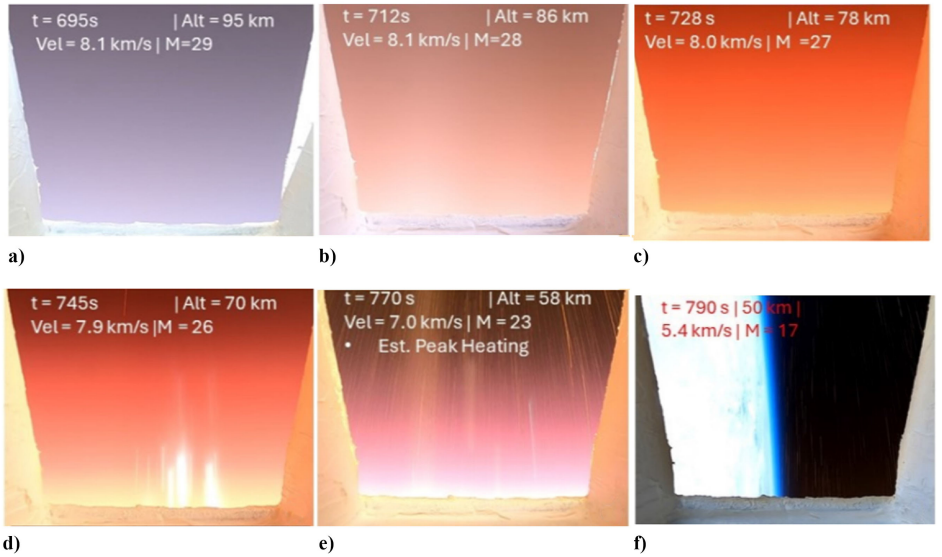

Fig. 10 GoPro camera footage along optical LOS taken during the W-1 reentry event with annotated time after separation, altitude, and speed [21].

and the energy state populations of these species produced by ablation interactions. The full effects of ablation products on the emitted radiance are currently under investigation, and will likely be completed once flight data is recovered to benchmark the results of available ablation solvers (e.g., Fully Implicit Ablation and Thermal response program). As the capsule slows down and approaches the estimated peak dynamic pressure point as in Fig. 10f, the plasma sheath subsides and no longer radiates visibly. This corresponds to the computed drop in radiance at 48 km, indicating that spectral emissions will not be resolvable in the Vis-NIR in this phase of the descent.

C. Spectrometer Response Calculation

A critical portion of the OSPREE payload development involved using the NEQAIR-generated synthetic spectra to determine the notional spectrometer response in counts along the trajectory for different spectrometer integration times. The workflow in Fig. 11 was implemented for these calculations. Spectra of a tungsten (blackbody) calibration lamp operating at 1800 K were taken with the fully assembled flight payload and optics using integration times (t_{int}) of 25, 50, 100, and 250 ms. Dividing the recorded spectrum at each t_{int} by the Planck distribution function using $T = 1800$ K for the spectrometer's wavelength range produced a set of system conversion factors (f_{sys}) to convert the NEQAIR computed spectral radiance to detector counts. Figure 12a shows the effect of varying t_{int} on the spectrometer response to the simulated radiance at 58 km. As expected, increasing the exposure time of the spectrometer results in a higher intensity spectral recording, with a two-order-of-magnitude difference in atomic oxygen peak intensity between 25 and 250 ms. The dashed horizontal line indicates the detector saturation limit at 65,535 counts; as the plasma sheath is more radiant toward the lower Vis, N_2^+ emission features in this region could oversaturate the detector when the highest integration time is used for collection. However, O emissions are better resolved with longer exposures and could be more useful for performing diagnostic calculations that involve mathematical methods such as Voigt fitting to extract the Stark broadening of the peak [32]. Thus, a longer t_{int} setting is preferred in regions where dissociation and atomic excitation occur.

The range of detectable response can be evaluated as in Fig. 12b, where the simulated response at each trajectory point is plotted for $t_{int} = 250$ ms. Even at the highest exposure time evaluated, the radiance emitted along the LOS at 98 km is not detectable by this system. A strong detector signal is expected between 85 and 52 km with minor saturation possible at the start of the spectral range between 70 and 58 km. At 52 km, the signal will be stronger in the lower Vis and drop off toward the IR. As the capsule slows down to the lower limit of the high hypersonic regime, the recorded intensity drops, and the radiance is not expected to be detectable below 48 km as the plasma sheath ceases to exist. The analysis of the simulated spectrometer response and uncertainties surrounding the increases in radiance from ablation products led to the decision to cycle the sensor through the four different exposure times throughout the entire flight. This data will provide the best postflight comparison of the effects of varying t_{int} across the entire trajectory. The Python controller script was programmed to take 40, 20, 10, and 4 recordings at respective t_{int} values of 25, 50, 100, and 250 ms and continuously cycle through these values from the start to the end of the recording period during descent. The saved spectral data files will be marked with a timestamp along with the integration time value used for the recording. This will allow for easier identification of the desired exposure time for ideal signal-to-noise ratio across the trajectory once flight data is recovered for analysis.

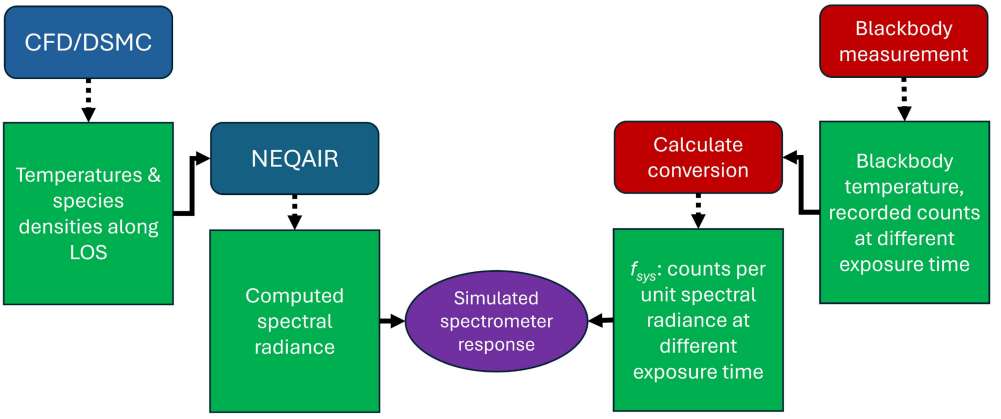

Fig. 11 Scheme of analysis procedure used to determine spectrometer response from NEQAIR computations.

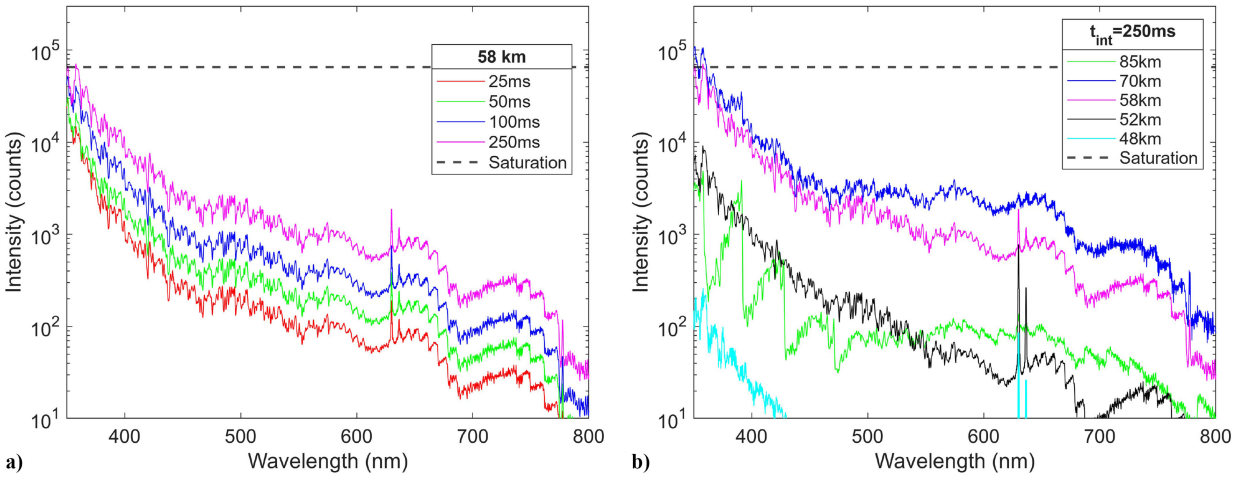

Fig. 12 Simulated spectrometer response a) at 58 km at different integration times and b) using 250 ms integration time across the trajectory.

V. Conclusions

An OES payload has been developed to record optical emissions of the plasma sheath around Varda's W-2 reentry capsule to better understand the dynamic chemical interactions that occur in this extreme environment. DSMC and CFD simulations of the flowfield yielded predictions of the chemical species and temperature distributions along the optical LOS, which were used to predict the spectral radiance incident on the sensor optics. Using calculated optical system conversion factors, the notional spectrometer response was determined from radiance computed along the capsule trajectory. The analysis indicates that spectral emissions will be detectable starting around 85 km and mostly dominated by N_2 and N_2^+. As the capsule enters continuum flow regimes, molecular dissociation will yield atomic oxygen emissions detectable with higher exposure times. Emissions will be detectable until the plasma sheath diminishes around 48 km. The data yielded from the OSPREE experiment provide invaluable chemistry information about the reentry plasma environment and will aid in the validation of computational reentry models in the high-hypersonic regime. Future work intended to be completed before the recovery of this payload will include the coupling of ablation models with the discussed CFD methods in order to better predict radiant signatures of molecules formed by the interaction of air with ablating TPS material. This will yield the best computational comparison to the experimentally recorded spectra and enable the validation of existing ablation modules in reentry Mach regimes.

Acknowledgments

This research was partially funded by an AFRL Edison grant as well as a Lab Task Grant from the Air Force Office of Scientific Research (24RVCOR005), supporting the scientific objectives of a funded effort between Varda and AFRL under contract FA-9453-23-C-A035. Engineering and qualification efforts were funded under contract FA-9453-18-D-0042 between AFRL and the Utah State University Space Dynamics Laboratory. Approved for public release; distribution is unlimited. Public Affairs release #AFRL-2024-6497. The views expressed are those of the author(s) and do not necessarily reflect the official policy or position of the Department of the Air Force, the Department of Defense, or the U.S. government.

References

[1] Petrova, T. B., Petrov, G. M., and Peñano, J. R., "Transport Properties of High Mach Number Hypersonic Air Plasmas," *Plasma Sources Science and Technology*, Vol. 33, No. 11, 2024, Paper 115008. https://doi.org/10.1088/1361-6595/ad8ef1

[2] Kulakhmetov, M. F., "Upscaling Ab-Initio Chemistry Models to Non-Equilibrium Flow Simulations," Ph.D. Thesis, Purdue Univ. Press, West Lafayette, IN, 2016.

[3] Park, C., and Griffith, G., "Nonequilibrium Hypersonic Aerothermodynamics," AIP Publishing, 1991.

[4] Vincenti, W. G., Kruger, C. H., Jr., and Teichmann, T., "Introduction to Physical Gas Dynamics," *Physics Today*, Vol. 19, No. 10, 1966, Paper 95.

[5] Bird, G., "The QK Model for Gas-Phase Chemical Reaction Rates," *Physics of Fluids*, Vol. 23, No. 10, 2011, Paper 106101. https://doi.org/10.1063/1.3650424

[6] Gallis, M. A., and Torczynski, J. R., "The Effect of Internal Energy on Chemical Reaction Rates as Predicted by Bird's Quantum-Kinetic Model," *AIP Conference Proceedings*, Vol. 1501, Nov. 2012, pp. 1051–1060. https://doi.org/10.1063/1.4769658

[7] Kulakhmetov, M., Gallis, M., and Alexeenko, A., "Ab Initio-Informed Maximum Entropy Modeling of Rovibrational Relaxation and State-Specific Dissociation with Application to the O2+ O System," *Journal of Chemical Physics*, Vol. 144, No. 17, 2016, Paper 174302. https://doi.org/10.1063/1.4947590

[8] Macdonald, R., Jaffe, R., Schwenke, D., and Panesi, M., "Construction of a Coarse-Grain Quasi-Classical Trajectory Method. I. Theory and Application to N2-N2 System," *Journal of Chemical Physics*, Vol. 148, No. 5, 2018, Paper 054309. https://doi.org/10.1063/1.5011331

[9] Gang Kim, J., and Boyd, I. D., "State-Resolved Thermochemical Nonequilibrium Analysis of Hydrogen Mixture Flows," *Physics of Fluids*, Vol. 24, No. 8, 2012, Paper 016101. https://doi.org/10.1063/1.4747340

[10] Erdman, P. W., Zipf, E. C., Espy, P., Howlett, C. L., Levin, D. A., Collins, R. J., and Candler, G. V., "Measurements of Ultraviolet Radiation From a 5-km/s Bow Shock," *Journal of Thermophysics and Heat Transfer*, Vol. 8, No. 3, 1994, pp. 441–446. https://doi.org/10.2514/3.562

[11] Levin, D., Candler, G., Collins, R., Erdman, P., Zipf, E., Espy, P., and Howlett, C., "Comparison of Theory with Experiment for the Bow Shock Ultraviolet Rocket Flight," *Journal of Thermophysics and Heat Transfer*, Vol. 7, No. 1, 1993, pp. 30–36. https://doi.org/10.2514/3.11565

[12] Kossi, K. K., and Boyd, I. D., "Detailed Computation of Ultraviolet Spectra in Rarefied Hypersonic Flow," *Journal of Spacecraft and Rockets*, Vol. 35, No. 5, 1998, pp. 653–659. https://doi.org/10.2514/2.3381

[13] Boyd, I., Phillips, W., Levin, D., Boyd, I., Phillips, W., and Levin, D., "Sensitivity Studies for Prediction of Ultra-Violet Radiation in Non-equilibrium Hypersonic Bow-Shock Waves," *35th Aerospace Sciences Meeting and Exhibit*, AIAA Paper 1997-131, 1997. https://doi.org/10.2514/6.1997-131

[14] Bose, D., and Candler, G. V., "Advanced Model of Nitric Oxide Formation in Hypersonic Flows," *Journal of Thermophysics and Heat Transfer*, Vol. 12, No. 2, 1998, pp. 214–222. https://doi.org/10.2514/2.6324

[15] Tacchi, B., Stoffel, T. D., Martin, A., and Poovathingal, S. J., "Reconstruction of the Kentucky Re-Entry Universal Payload System Hypersonic Flight Trajectory," *Journal of Spacecraft and Rockets*, Vol. 61, No. 2, 2024, pp. 438–447. https://doi.org/10.2514/1.A35826

[16] Ruffner, M. P., Ford, K. F., Craig, L. M., Tacchi, B. D., Schmidt, J. D., Poovathingal, S. J., Smith, W. T., and Martin, A., "Overview of the Hypersonic Test Flight KREPE-2," *AIAA Aviation Forum and Ascend 2024*, AIAA Paper 2024-3561, 2024. https://doi.org/10.2514/6.2024-3561

[17] Lein, S., Steinbeck, A., Preci, A., Fertig, M., Herdrich, G., Röser, H.-P., and Auweter-Kurtz, M., "Final Design and Performance Parameters of the Payloads PYREX, PHLUX and RESPECT on EXPERT," *Transactions of the Japan Society for Aeronautical and Space Sciences, Aerospace Technology Japan*, Vol. 8, No. ists27, 2010, pp. Tm_41–Tm_47.

[18] Winter, M., Fertig, M., and Auweter-Kurtz, M., "Status of the Re-Entry Spectrometer System RESPECT as a Payload on the European Re-Entry Capsule EXPERT," *4th International Symposium Atmospheric Reentry Vehicles and Systems*, Arcachon, France, March 2005.

[19] Lein, S., Reimer, T., Stubicar, K., Deuble, F., Auweter-Kurtz, M., Herdrich, G., and Winter, M., "Development of the Re-Entry Spectrometer RESPECT for the ESA Capsule EXPERT," *Acta Astronautica*, Vol. 64, No. 4, 2009, pp. 416–426. https://doi.org/10.1016/j.actaastro.2008.07.024

[20] Kulakhmetov, M. F., Alviani, R., Rao, A., Murray, V., Taylor, J. B., Seik, J., and Vaughan, E., "Optimizing Optical Emission Measurements on the Varda Hypersonic Testbed Vehicle," *AIAA Aviation Forum and ASCEND 2024*, AIAA Paper 2024-4560, 2024. https://doi.org/10.2514/6.2024-4560

[21] Varda Space Industries, "Varda Capsule Reentry—Full Video from LEO to Earth," 2024, https://youtu.be/BWxl921rMgM?si=KXp1-3YJzX-oZm7K.

[22] Guertin, S. M., *Raspberry Pis for Space Guideline*, NASA, Washington, DC, USA, 2022.

[23] SPARTA, *SPARTA Users Manual*, Sandia National Lab., Albuquerque, NM, Sept. 2024.

[24] LAURA, *Langley Aerothermodynamic Upwind Relaxation Algorithm, Software Package*, Ver, 5.6, NASA Langley Research Center Hampton, Hampton, VA, 2020.

[25] Bird, G. A., *Molecular Gas Dynamics and Simulation of Gas Flows*, Cambridge Univ. Press, Cambridge, England, U.K., 1994.

[26] Valentini, P., Verhoff, A. M., Grover, M. S., and Bisek, N. J., "First-Principles Predictions for Shear Viscosity of Air Components at High Temperature," *Physical Chemistry Chemical Physics*, Vol. 25, No. 13, 2023, pp. 9131–9139. https://doi.org/10.1039/D3CP00072A

[27] Valentini, P., Zhang, C., and Schwartzentruber, T. E., "Molecular Dynamics Simulation of Rotational Relaxation in Nitrogen: Implications for Rotational Collision Number Models," *Physics of Fluids*, Vol. 24, No. 10, 2012, pp. 106101. https://doi.org/10.1063/1.4757119

[28] Torres, E., Geistfeld, E. C., and Schwartzentruber, T. E., "High-Temperature Nonequilibrium Air Chemistry from First Principles,"

Journal of Thermophysics and Heat Transfer, Vol. 38, No. 2, 2024, pp. 1–32.
https://doi.org/10.2514/1.T6863

[29] Shevyrin, A. A., Wu, J.-S., and Bondar, Y. A., "Investigation of an Ionized Shock Layer in a Rarefied Gas Flow Around a Reentry Vehicle," *AIP Conference Proceedings*, Vol. 1770, Oct. 2016, Paper 040011.
https://doi.org/10.1063/1.4964080

[30] Farbar, E., Boyd, I. D., and Martin, A., "Numerical Prediction of Hypersonic Flowfields Including Effects of Electron Translational Nonequilibrium," *Journal of Thermophysics and Heat Transfer*, Vol. 27, No. 4, 2013, pp. 593–606.
https://doi.org/10.2514/1.T3963

[31] Clarey, M. P., and Greendyke, R. B., "Investigation of Thermochemical Non-Equilibrium Phenomena in the Wake of a Hypersonic Vehicle Using Three-Temperature Models," *AIAA Scitech Forum*, AIAA Paper 2018-0744, 2018.
https://doi.org/10.2514/6.2018-0744

[32] Rao, A. P., Nawar, N., and Annesley, C. J., "Time-Resolved Diagnostic Measurements of Sub-Atmospheric Laser-Induced Air Plasmas Using the OI 777 nm Emission," *Optics Continuum*, Vol. 3, No. 2, 2024, pp. 187–199.
https://doi.org/10.1364/OPTCON.511770

R. Cummings
Associate Editor